Biomaterials 31 (2010) 7534–7541

Contents lists available at ScienceDirect

Biomaterials

journal homepage: www.elsevier.com/locate/biomaterials

# The application of complex multiple forklike ZnO nanostructures to rapid and ultrahigh sensitive hydrogen peroxide biosensors

Zao Yang [a,*], XiaoLing Zong [b], Zhizhen Ye [a], Binghui Zhao [a], QingLing Wang [a], Ping Wang [b]

[a] Department of Materials Science and Engineering, State Key Laboratory of Silicon Materials, Zhejiang University, Hangzhou 310027, China
[b] Biosensor National Special Laboratory, Key laboratory of Biomedical Engineering of National Education Ministry, Department of Biomedical Engineering, Zhejiang University, Hangzhou 310027, China

ARTICLE INFO

*Article history:*
Received 14 March 2010
Accepted 6 June 2010
Available online 2 July 2010

*Keywords:*
Electrochemistry
Crystal growth
Biosensor
Enzyme

ABSTRACT

A new complex multiple forklike ZnO nanostructure was fabricated by citric acid assisted annealing process. The complex multiple forklike ZnO nanostructure is composed of several nanorods. These nanorods grow from a thin platelet base and are parallel to each other to form complex multiple forklike ZnO nanostructure. The widthes of thin platelet bases range from 60 to 230 nm. The diameters of the nanorods range from 16 to 60 nm, and their lengths are 0.5 μ∼ 1.3μ. FT-IR spectrum, room-temperature PL, and UV–Vis absorption spectra are also discussed. A possible growth mechanism is proposed. Complex multiple forklike ZnO nanostructure was first used to construct a novel enzymatic biosensor based on the ZnO/CHIT inorganic–organic composite film. Well-studied horseradish peroxidase (HRP) was chosen as a model enzyme. The as-prepared biosensor displays ultrahigh sensitivity, quick response time, low detection limit and small apparent Michaelis–Menten constant. These results show that the Complex multiple forklike ZnO nanostructure is a promising material to construct enzyme biosensors.



## 1. Introduction

The design of nanoscale materials with controlled size and morphology has stimulated considerable research efforts in seeking new morphology-physical properties and functions. As is well-known, different morphologies can have a large effect on the properties of nanostructures themselves. Complex nanostructures of, typically, II–VI and III–V semiconductors have been a new focus in nanoscience because of their exciting optical and electronic properties, which are closely related to their unique morphologies and spatial organization. What's more, complex nanostructure materials are also expected to represent important building blocks for nanoscale devices possessing various interesting functions. Self-assembly driven by physical or chemical interaction is an effective route to construct nanoscale materials with a multidimensional (MD) structure.

ZnO is an important group II–VI semiconductor with a wide bandgap (3.37 eV) and a large exciton binding energy of 60 meV at room temperature [1]. It is one of the many technologically important semiconducting materials with a variety of applications, including chemical sensor [2], catalysts [3], UV light-emitters [4], phosphors [5], photovoltaics [6], cantilevers [7], varistors [8]. Recently, a variety of ZnO nanostructures have been synthesized by various physical and chemical routes. The synthesis of ZnO nanostructure ranging from wires [9], rods [10], belts [11], tubes [12], coaxial cables [13], branches [14], needles [15], towers [16], columns [17], tetrapods [18], nail [19], helices [20], combs [21], cones [22], and paint-brush structures [23], has attracted considerable research interest because of their great potential for fundamental studies of the roles of dimensionality and size in their physical properties as well as for applications of building blocks and interconnects in electronic and photonic devices. Generally, the fabrication methods for ZnO nanostructures can be divided into two groups: "hard" and "soft" approaches. The former includes template-directed synthesis, the vapor–liquid–solid (VLS), vapor–solid (VS) techniques, which usually require high temperature, high pressure, substrate choice, and low product yield. The latter, "soft" approaches, such as hydrothermal/solvothermal processes, the solution–liquid–solid (SLS) mechanism, and capping agents/surfactant-assisted synthesis, provide a convenient and lower-temperature pathway for the fabrication of desired ZnO nanostructures. Although substantial effort has been devoted to the development of new synthetic methodologies for making new nanostructures, achieving control over the size and morphology of the grown ZnO nanostructures and their further self-organization into MD structures in large scale at low cost is still challenging. In

* Corresponding author. Tel.: +86 571 8795 3139; fax: +86 571 8795 2625.
*E-mail address:* yangzao888@tom.com (Z. Yang).

0142-9612/$ – see front matter © 2010 Published by Elsevier Ltd.
doi:10.1016/j.biomaterials.2010.06.019

addition, the large-scale industrial preparation of MD ZnO nanomaterials by a controlled methodology is very difficult. Hence, it is fundamentally and practically important to exploit a quick, simple, and scale-up easy synthetic method for growing new complex MD nanostructures at low cost.

In the area of bioscience, the special properties of ZnO nanostructure have also attracted much attention gradually. ZnO is a good biomaterial with a high Isoelectric Point (IEP) of ~9.5 which makes it suitable for absorption of proteins with low IEPs where the protein immobilization is primarily driven by electrostatic interaction [24]. ZnO possesses several unique advantages such as high-specific surface area, nontoxicity, chemical stability, electrochemical activity, and high electron communication features. Such properties indicate the potential applications of ZnO as one of the promising materials for biosensor applications [25]. So far, ZnO nanoparticles, porous films, nanocombs, and nanorods have been developed into biosensors to detect cytochrome C [26], protein [27], uric acid [28], glucose [29], and phenolic compounds [30], respectively. Over the past decades, the determination of hydrogen peroxide ($H_2O_2$) has been a very active study area because $H_2O_2$ plays an important role in food industry, environmental monitoring and clinical diagnosis. Moreover, the electrochemical tracking of biological targets by way of enzyme-based $H_2O_2$ detection is of special interest. However, hydrogen peroxide biosensor made of ZnO nanostructures is rare. There are only two reports in the literature in which ZnO nanostructures are used in hydrogen peroxide biosensor [31,32]. The lower sensitivity and higher detection limit of previously fabricated ZnO nanostructures based hydrogen peroxide biosensor has been demonstrated in the literature, hence more works are needed to obtain the higher-sensitivity and lower-detection limit of the ZnO nanostructures based hydrogen peroxide biosensors. To the best of our knowledge, there is no report on investigating complex multiple forklike ZnO nanostructures based hydrogen peroxide biosensors.

In this paper, we first report a new complex multiple forklike ZnO nanostructure. It is synthesized by citric acid assisted annealing process. The samples are characterized by X-ray diffraction (XRD), field-emission scanning electron microscopy (FE-SEM), high-resolution transmission electron microscopy (HRTEM), FT-IR spectrophotometer, photoluminescence (PL) spectroscopy, ultraviolet visible (UV–Vis) spectroscopy. Complex multiple forklike ZnO nanostructure was first used to construct an enzymatic biosensor based on the ZnO/CHIT inorganic–organic composite film. Well-studied horseradish peroxidase (HRP) was chosen as a model enzyme.

## 2. Experimental section

### 2.1. Synthesis of complex multiple forklike ZnO nanostructure

All the chemicals used in this study were of analytical grade and used without further purification. Four chemicals were needed and they were analytically pure zinc acetate (Zn $(CH_3COO)_2{\cdot}2H_2O$, citric acid ($C_6H_8O_7{\cdot}H_2O$), pure distilled water ($H_2O$) and absolute ethanol ($CH_3CH_2OH$). A solution of citric acid (0.16 M) in ethanol was added to Zn $(CH_3COO)_2$ solutions (1.8M) in distilled water. After the addition was finished, the solution (pH value was equal to 5.8) was stirred at 80 °C for 9 h to get the precursor. The precursor was calcined in a muffle furnace for 2 h at 400 °C. After heat treatment, the powder was cooled naturally down to room temperature in air.

### 2.2. Material characterization

The obtained sample was characterized by X-ray powder diffraction XRD (Rigaku, $D/_{max}$-rA) with Cu Kα radiation. The size and morphology of as-synthesized sample were determined using a HITACHI S-4800 scanning electron microscope, JEM-2010 high-resolution transmission electron microscope. EDX was performed to determine the composition of the products. Infrared (IR) absorption spectroscopy (Nicolet Nexus 670) was carried out at room temperature in the range of 400–4000 $cm^{-1}$ by FT-IR spectrophotometer. Photoluminescence (PL) measurements were performed at room temperature by using a He–Cd laser (325 nm) as the excitation source. UV–Vis absorption spectra were recorded using a Unico UV–Vis 2802 PC spectrophotometer.

### 2.3. Fabrication of hydrogen peroxide biosensors

The $H_2O_2$ biosensor used in this study was fabricated as follows: the glassy carbon (GC) electrodes was polished by 0.3 and 0.05 μm aluminum slurries and then was cleaned by dipping into 1:1(V/V) aqueous solution of $HNO_3$, deionized water and ethanol with the assistance of ultrasonication prior to the experiment. The as-prepared Complex multiple forklike ZnO nanostructures were dispersed, in ethanol by ultrasonication for 1 h to $5 \times 10^{-3}$ M suspension. Firstly, 5 μl of complex multiple forklike ZnO nanostructure suspension was firstly dropped onto the surface of GC electrode and dried at room temperature. Secondly, 5 μl of HRP (E.C.1.11.1.7, RZ > 3.0, A > 250 U $mg^{-1}$) Solutions with concentration of 5.0 mg $ml^{-1}$ prepared in 0.067M phosphate buffer (pH 7.0) was dropped onto the surface of GC electrode modified by complex multiple forklike ZnO nanostructure. Finally, 5 μl of 0.5 wt% CHIT (molar weight ~ $1 \times 10^6$, 75–85% deacetylation) solution dissolved in acetic acid solution was dropped onto the surface of HRP/complex multiple forklike ZnO nanostructures/GC to avoid the leakage of the enzyme. The device was dried at 4 °C overnight in a refrigerator, followed by washing step to remove the unimmobilized HRP. The CHIT/HRP/complex multiple forklike ZnO nanostructures/GC electrode was stored in PBS and kept at 4 °C in a refrigerator when not in use.

## 3. Results and discussion

### 3.1. Synthesis and structure of the complex multiple forklike ZnO nanostructure

A typical XRD pattern of the product is shown in Fig. 1. All the diffraction peaks can be indexed as a wurtzite structure ZnO ($a = 0.3249$ nm, $c = 0.5205$ nm, space group: $P_63mc$ (186)) with high crystallization, which together with the intensity distribution are consistent with those of the standard card for the hexagonal ZnO crystal (Joint Committee for Powder Diffraction Studies (JCPDS) 36-1451). No characteristic peaks were observed for impurities. The XRD patterns indicate that the samples obtained via our current synthetic methods consist of pure phases.

The characteristic morphology of the complex multiple forklike ZnO nanostructure can be seen in the field-emission scanning electron microscopy (FE-SEM) images shown in Fig. 2. Fig. 2(a) is a low-magnification picture of complex multiple forklike ZnO nanostructure. It illustrates that the products are composed of several nanorods. Fig. 2(b) is a medium magnification picture of complex multiple forklike ZnO nanostructure. Interestingly, these nanorods grow from a thin platelet base and are parallel to each other to form complex multiple forklike ZnO nanostructure. The widthes of thin platelet bases range from 60 to 230 nm. The diameters of the nanorods range from 16 to 60 nm, and their

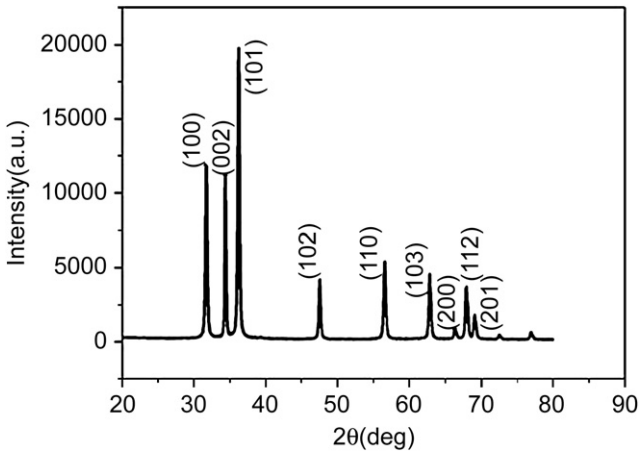


**Fig. 1.** XRD patterns of as-grown complex multiple forklike ZnO nanostructure.

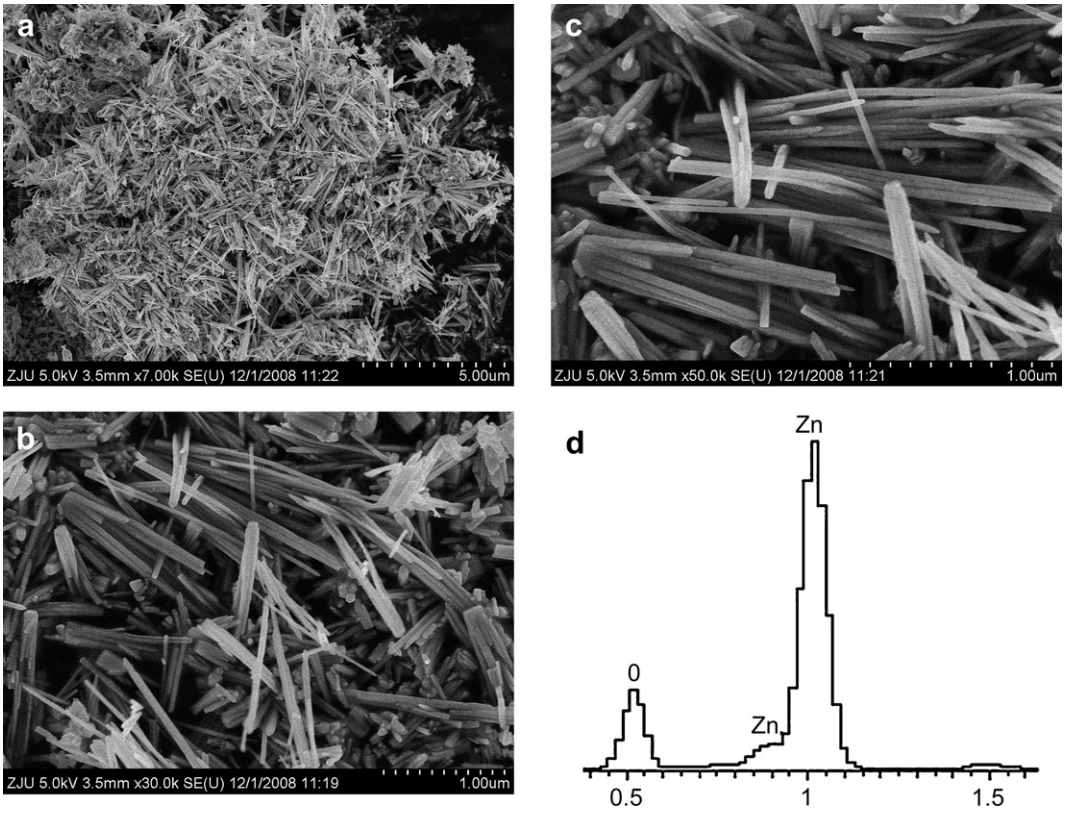


**Fig. 2.** (a) A low-magnification picture of complex multiple forklike ZnO nanostructure. (b) A medium magnification picture of complex multiple forklike ZnO nanostructure. (c) A high-magnification FE-FEM image of complex multiple forklike ZnO nanostructure. (d) EDS of complex multiple forklike ZnO nanostructure.

lengths are 0.5μ ~ 1.3μ. Furthermore, both ends of the nanorods have relatively smaller diameters compared with the central parts, as seen in the high-magnification FE-FEM image (Fig. 2(c)). More careful observation of the morphology of complex multiple forklike ZnO nanostructures indicated that the nanorods grew on the side surface of thin platelet base. The EDS result (Fig. 2(d)) shows only Zn and O Peaks for the samples. No other elements were detected from the samples. XRD, EDS and SEM results demonstrate that the product is a single-crystalline ZnO nanostructure without defects or dislocations.

Further detailed structural analysis of complex multiple forklike ZnO nanostructure was carried out using transmission electron microscopy (TEM). Typical TEM image obtained from the sample is shown in Fig. 3(a). It indicates that each nanorod of complex multiple forklike ZnO nanostructure has uniform diameters and no catalyst particle at the tip. The surface of the nanorods is very smooth. Each nanorod has shrinking necks with sharp tips. The surface of the nanorods and the junction were both very smooth. The edges of the nanorod are clear, and no amorphous layer is observed on the surface. The junction parts are further detailed in Fig. 3(b). These crystals show joinable capacity for further assemblies with other nanostructures (including heteronanostructures), especially for creating an external connectivity (thin platelet base). To gain detailed structural information for complex multiple forklike ZnO nanostructure, high-resolution TEM (HRTEM) image is also recorded on a single rod of complex multiple forklike ZnO nanostructure. The HRTEM image from one nanorod is shown in Fig. 3 (c). The lattice spacing of 0.263 nm corresponds to the ZnO crystal planes, which indicates that the ZnO each rod of complex multiple forklike ZnO nanostructure is preferentially oriented along the [0001]. Each rod of complex multiple forklike ZnO nanostructure possesses a single-crystal hexagonal structure without dislocations and stacking faults. ZnO nanostructures are easily synthesized owing to facile growth along the *c* axis of the wurtzite crystal, which has a hexagonal unit cell with six nonpolar $\{10\bar{1}0\}$ prismatic faces capped by polar oxygen $(000\bar{1})$ and zinc (0001) basal planes. The polar faces are electrostatically unstable Tasker type III surfaces [33], making the {0001} planes has the highest energy of the low-index surfaces. This suggests a growth habit where the *c* axis is the fastest-growing direction.

The possible growth mechanism is given below. We begin to study from Gibbs–Thompson equation:

$$S_r = S_b \exp\left(\frac{2\sigma V_m}{rRT}\right) \quad (1)$$

Where $r$ is the radius of the crystal, $\sigma$ is the specific surface energy, $V_m$ is the molar volume of the material, $S_b$ and $S_r$ are the solubilities of bulk crystals and crystals with a radius $r$, respectively, $R$ is the gas constant, and $T$ is the absolute temperature. In principle, the higher the monomer concentration is, the smaller the critical nuclei can be, the easier the nucleation process can take place. The inevitable formation of critically sized nanoclusters in the nucleation stage for the growth of anisotropic shapes likely plays a key role in determining the nature of all of the following events, and the size/shape of the resulting nanocrystals [34]. The critically sized nuclei deeply impact the following growth process of the elongated nanostructures. A relatively high monomer concentration will promote to grow longer in the following one dimension growth. Conversely, a relatively low monomer concentration will promote two-dimension or multidimensional grows [35], so complex multiple forklike ZnO nanostructure is formed.

The ZnO samples were mixed with potassium bromide in the ratio of 1:100. The background spectrum recorded using KBr was

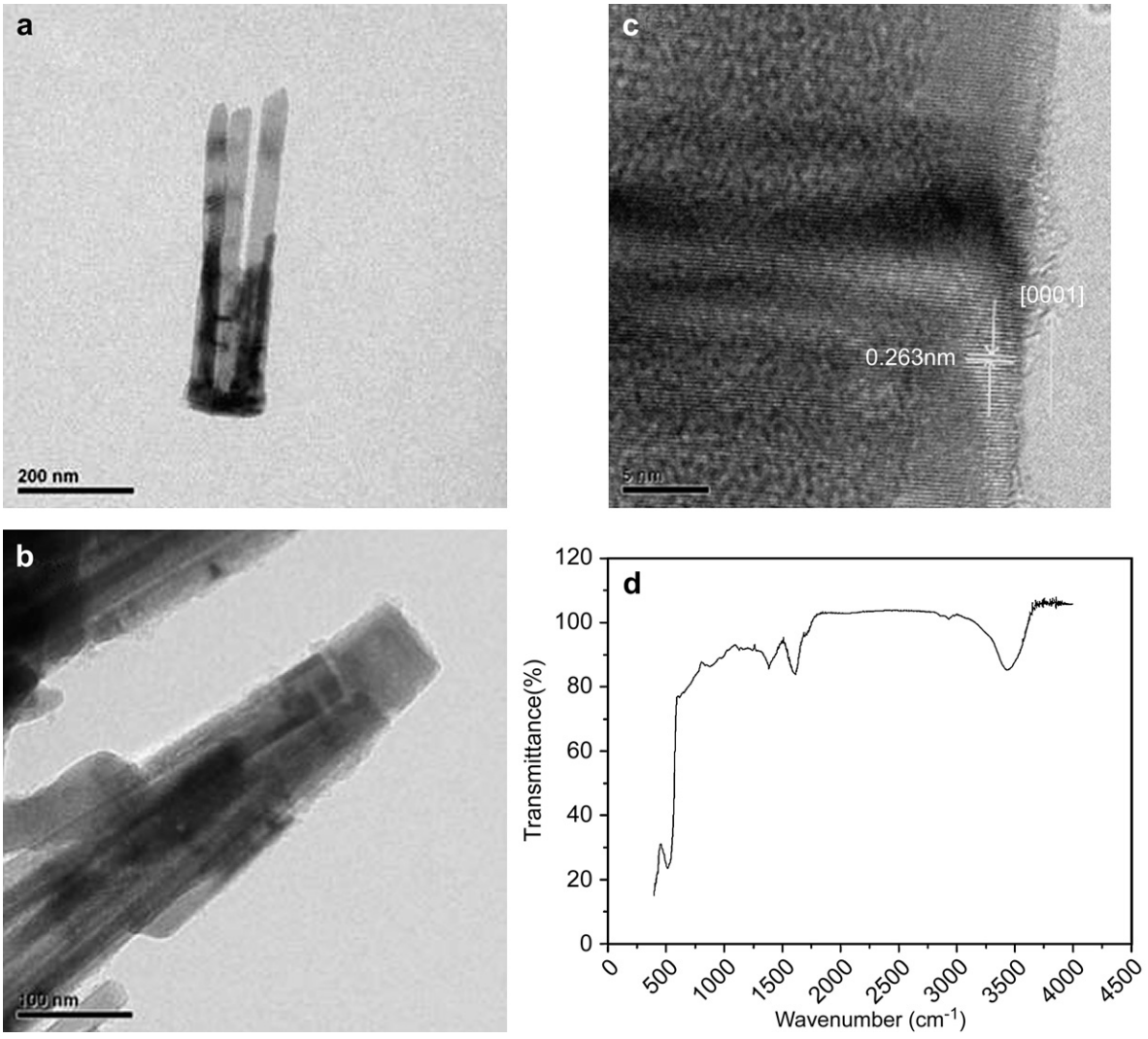


**Fig. 3.** (a) Typical TEM image of complex multiple forklike ZnO nanostructure (b) TEM image of junction parts of complex multiple forklike ZnO nanostructure (c) HRTEM image of a single rod of complex multiple forklike ZnO nanostructure (d) IR spectra for complex multiple forklike ZnO nanostructure.

subtracted from the sample spectrum. Fig. 3(d) exhibits IR spectra for the as-obtained ZnO nanostructure. In the IR spectra, spherical ZnO nanoparticle usually shows one distinct absorption bands at around 464 $cm^{-1}$ [36]. The position and number of these bands not only depend on crystal structure and chemical composition but also on particle morphology [37]. If the particle morphology changes from spherical to a needlelike shape, this maximum broadens and splits into two maxima absorption bands at around 512 and 406 $cm^{-1}$ [36]. These absorption peaks locate between the bulk TO-phonon frequency ($\omega T_{\perp}$) and the LO-phonon frequency ($\omega_I L_{II}$). In Fig. 3(d), the IR spectrum of the complex multiple forklike ZnO nanostructure shows a characteristic absorption band at $\sim$508 $cm^{-1}$ and there will be another absorption band at 432 $cm^{-1}$. These absorption peaks shifted towards lower frequencies when the permittivity of the surrounding medium was increased.

### 3.2. Optical properties of the complex multiple forklike ZnO nanostructure

The PL from ZnO consists of two emission bands at room temperature: a near-band-edge (UV) emission and a broad, deep-level (visible) emission. For bulk ZnO crystals, ultraviolet emissions were only observed at very low temperature, while the intensity of the emissions was found to decrease rapidly with the increase of temperature due to the thermal quenching effect. It was therefore difficult to observe UV light emission from bulk ZnO at ambient temperature. Two factors were responsible for the enhancement in emission intensity of the room temperature PL. One was the high-quality of ZnO nanostructure. On the other hand, the quantum confinement effect related to the nanostructures was another important factor responsible for the increase of emission intensity of the observed UV emission at room temperature. The visible emission is usually considered to be related to various intrinsic defects produced during ZnO preparation [38]. Normally, these defects are located at the surface of the ZnO nanostructure [39]. The green emission of ZnO is usually ascribed to structural defects, which included zinc vacancy ($V_{Zn}$), oxygen vacancy ($V_O$), interstitial zinc ($Zn_i$), interstitial oxygen ($O_i$) and antisite oxygen ($O_{Zn}$). Fig. 4(a) shows the room-temperature PL spectra of complex multiple forklike ZnO nanostructure. This is only one emission peak in the UV region at 384 nm. The UV emission attributes to the near-band-edge emission, arises from the recombination of free excitons through an excition–exciton collision process [40]. This indicates that the ZnO samples have better crystal quality.

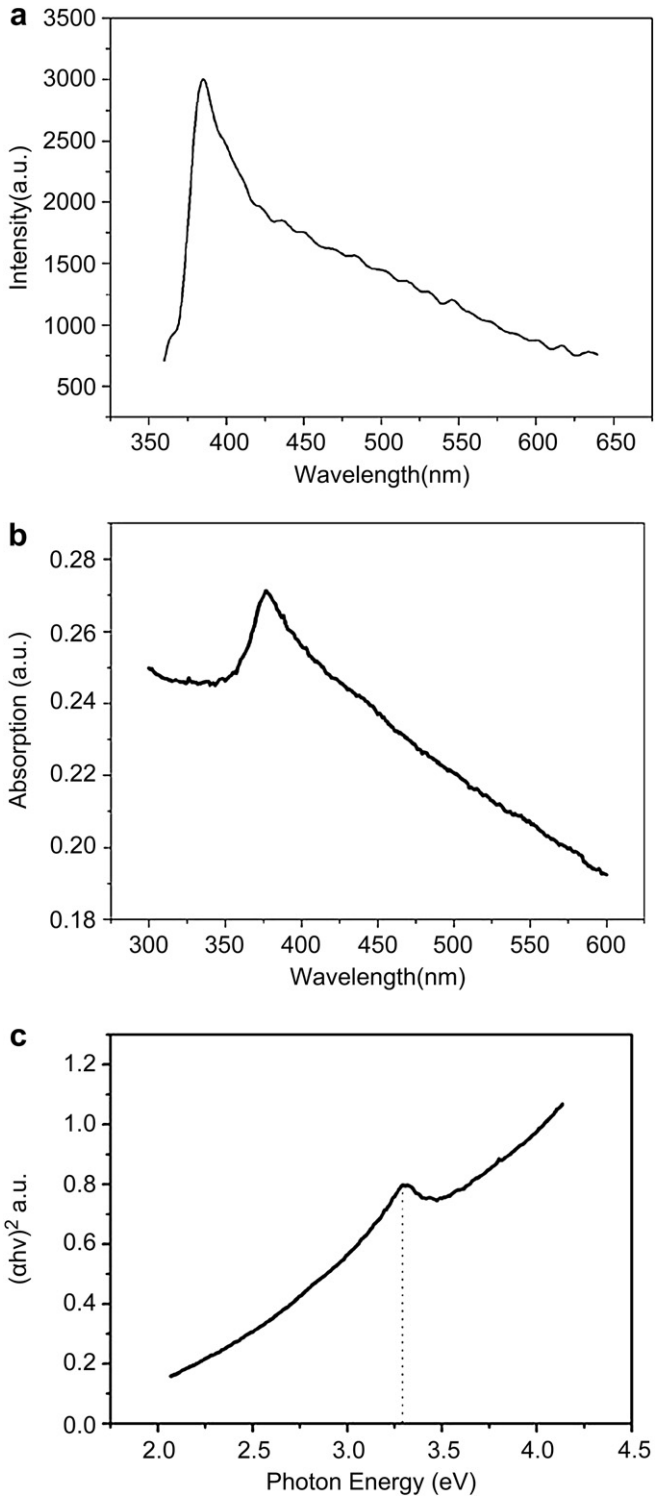


**Fig. 4.** (a) the room-temperature PL spectra of complex multiple forklike ZnO nanostructure (b) the UV–Vis absorption spectra of the complex multiple forklike ZnO nanostructure at room temperature (c) plot of $(\alpha h\nu)^2$ as a function of photon energy $E_g$ for the complex multiple forklike ZnO nanostructure.

The UV–Vis absorption spectra of the complex multiple forklike ZnO nanostructure at room temperature are shown in Fig. 4(b). The absorption spectra have a peak near the band edge in the exciton absorption region (at about 377 nm) and blue-shifted relative to the bulk exciton absorption (380 nm). The reason being the carriers are confined in a very small district that makes the electron and hole move only in a potential well. At the same time, it can enhance the coupling interaction with each other. Then the exciton bounded stronger and probability of binding increased, so we can observe a more apparent exciton absorption peak and hence the blue shift occurred. The direct bandgap energy ($E_g$) for the ZnO powders is determined by fitting the absorption data to the direct transition equation:

$$\alpha h\nu = E_D(h\nu - E_g)^{1/2} \quad (2)$$

Where $\alpha$ is the optical absorption coefficient, $h\nu$ is the photon energy, $E_g$ is the direct bandgap, and $E_D$ is a constant [41]. Plotting $(\alpha h\nu)^2$ as a function of photon energy, and extrapolating the linear portion of the curve to absorption equal to zero as shown in Fig. 4 (c), gives the value of the direct bandgap ($E_g$) to be 3.28 eV.

### 3.3. Application as hydrogen peroxide biosensor

Complex multiple forklike ZnO nanostructure was used to construct a enzymatic biosensor based on the ZnO/CHIT inorganic–organic composite film as the immobilization matrix. The fabrication process of the enzyme electrode is schematically illustrated in Fig. 5. The as-prepared biosensor displayed high sensitivity, quick response to $H_2O_2$ and good stability. The cyclic voltammetric behavior of the enzyme electrode in an unstirred 0.067M phosphate buffer solution (pH 7.0) containing 1.0 mm hydroquinone without $H_2O_2$ and with 1.05 mM $H_2O_2$ added was investigated at a scan rate of 100 $mVs^{-1}$ shown in Fig. 6. Fig. 6(a) is the cyclic voltammetric responses of GC/Complex multiple forklike ZnO nanostructure/CHIT/HRP electrode in stirred 0.067M PBS (pH 7.0) in the absence of hydroquinone. No electrochemical response is observed. In the absence of $H_2O_2$, the HPR electrode only gives the electrochemical behavior of hydroquinone in solution and there is a pair of typical oxidation and reduction peaks (Fig. 6(b)); The results indicate that hydroquinone could be used as a diffusional

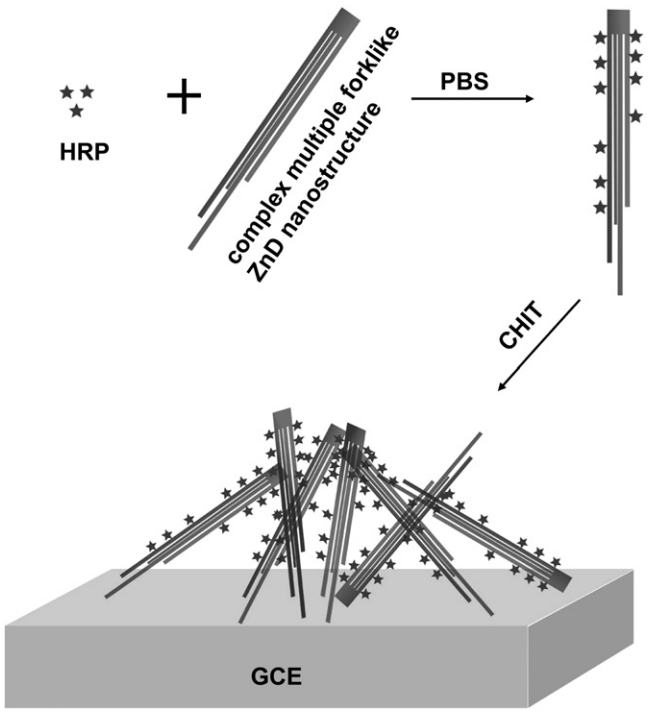


**Fig. 5.** Schematic illustration of the preparation process of the enzyme electrode.

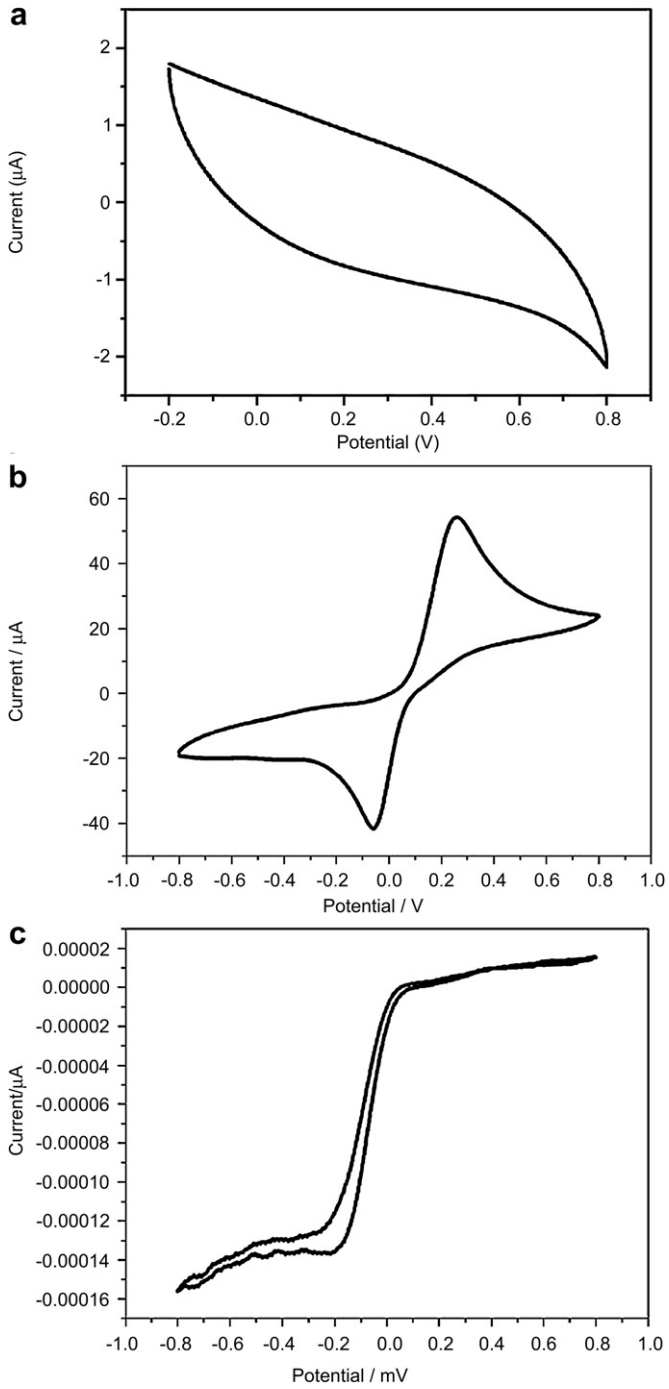


**Fig. 6.** (a) the cyclic voltammetric responses of GC/Complex multiple forklike ZnO nanostructure/CHIT/HRP electrode in stirred 0.067M PBS (pH 7.0) in the absence of hydroquinone (b) the cyclic voltammetric responses of GC/Complex multiple forklike ZnO nanostructure/CHIT/HRP electrode in stirred 0.067M PBS (pH 7.0) containing 1.0 Mm hydroquinone without $H_2O_2$ (c) the cyclic voltammetric responses of GC/Complex multiple forklike ZnO nanostructure/CHIT/HRP electrode in stirred 0.067M PBS (pH 7.0) containing 1.0 Mm hydroquinone with 1.05 mM $H_2O_2$ added; scan rate 100 $mVs^{-1}$.

electron-transferring mediator. The addition of 1.05 mM $H_2O_2$ results in an increase in the reductive current and a decrease in the oxidative current (Fig. 6(c)). This indicated that the current response was catalyzed by HRP. It may be attributed that the synergistic effect between ZnO and hydroquinone is preferable for the enzyme and promote the electron transfer between the protein and electrode. These phenomena indicated the hydroquinone could effectively shuttle electrons from GC electrode surface to the redox center of HRP immobilized on the complex multiple forklike ZnO nanostructure. The typical enzyme-dependent catalytic process can be expressed as follow [42]:

$$\text{HRP } (Fe^{3+}) + H_2O_2 \rightarrow \text{Compound (I)} + H_2O \quad \text{(a)}$$

$$\text{Compound (I)} + QH_2 \rightarrow \text{Compound (II)} + Q \quad \text{(b)}$$

$$\text{Compound (II)} + QH_2 \rightarrow \text{HRP } (Fe^{3+}) + Q + H_2O \quad \text{(c)}$$

$$Q + 2e \rightarrow QH_2 \quad \text{(d)}$$

Where compounds I (oxidation state + 5) and II (oxidation state + 4) represent intermediates in the reactions and $QH_2$, Q repreents hydroquinone and its oxidized form (benzoquinone), respectively. Compound I was reduced to compound II, and then II to the original form of HRP ($Fe^{3+}$) by a redox mediator $QH_2$. The benzoquinone is subsequently reduced back to hydroquinone by a rapid reaction involving the acceptance of two electrons from the electrode. The reason that the ZnO/CHIT inorganic–organic composite film could facilitate the electron transfer between the protein molecules and the electrode could be elucidated as follows. Firstly, as we have mentioned, the good biocompatibility of the composite film may prevent denaturation and retain the essential secondary structure of the entrapped protein. More importantly, due to its high surface area, the complex multiple forklike ZnO nanostructure can enhance the active surface area of the GC electrode available for protein binding; meanwhile, the complex multiple forklike ZnO nanostructure may probably act a rigid framework to favor the appropriate conformation of entrapped proteins, facilitating the electron transfer between the redox protein and the underlying electrode.

Fig. 7(a) displays the typical current–time response of the biosensor on successive step changes of 0.5 mm $H_2O_2$ in 0.067M PBS buffer (pH = 7.0) at an applied potential of −0.2 V under stirring. It is found that the biosensor shows a rapid and sensitive response to the change of $H_2O_2$ concentration, which is ascribed to the good electrocatalytic property of CHIT/$GO_x$/ZnO/GC electrode. The detection limit of the sensor was found to be 0.3 μm. The biosensor could achieve 95% of the steady-state current within 3 s. It indicated that the immobilized HRP could well catalyze the reduction of $H_2O_2$, which was due to the fact that the uniform complex multiple forklike nanostructure of the ZnO matrix yields a very low mass transport barrier and results in a rapid diffusion from bulk solution to enzyme and the complex multiple forklike ZnO nanostructure could effectively retain the bioactivity of the HRP. The corresponding calibration curve is shown in Fig. 7(b). The linear detection range of complex multiple forklike ZnO nanostructure-based $H_2O_2$ biosensor is $5 \times 10^{-5}$M to $7 \times 10^{-4}$ M with a correction coefficient $R = 0.9979$. This kind of biosensor has a low detection limit of 0.3 μm. The reduction of $H_2O_2$ could be well catalyzed by the immobilized HRP, which was due to the fact that the complex multiple forklike ZnO nanostructure provided a mild immobilization process for HRP, effectively retain its bioactivity and enhanced the electron transfer between the enzyme active sites and the electrode. The sensitivity of our biosensor is determined to be as high as 201.12 μAm $M^{-1}$, better than many previous reports [31,32]. It indicated the enzyme electrode had good bioelectrocatalytic activity for $H_2O_2$. The apparent Michaelis–Menten constant ($K_m^{app}$) could be calculated from the Lineweaver–Burk equation [43]:

$$1/I_{SS} = 1/I_{max}(1 + K_m^{app}(mM)/C) \quad (3)$$

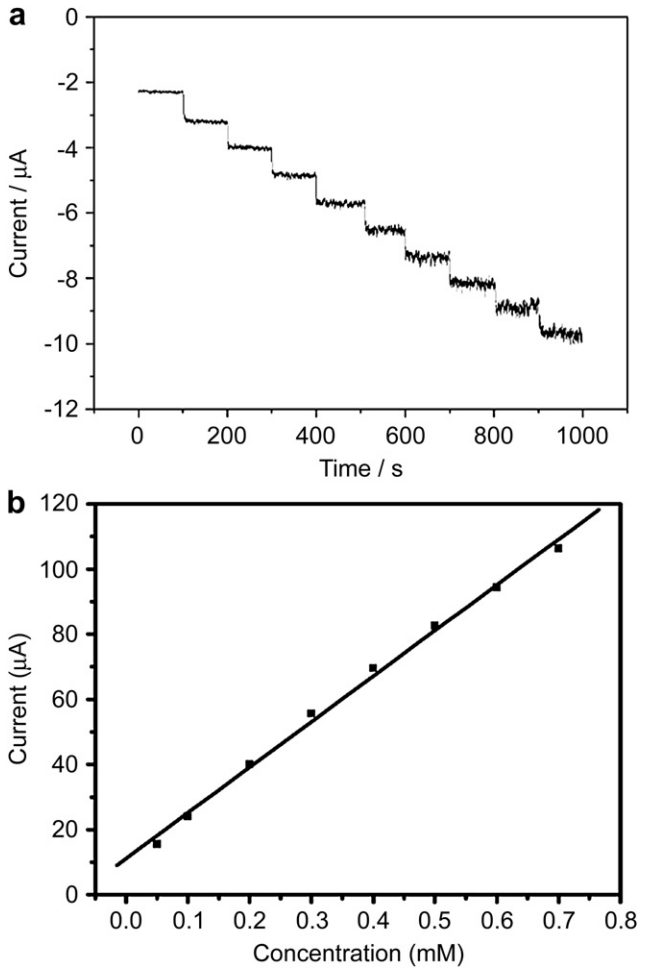


**Fig. 7.** (a) the typical current–time response of the biosensor on successive step changes of 0.5 mm $H_2O_2$ in 0.067M PBS buffer (pH = 7.0) at an applied potential of −0.2 V under stirring (b) The corresponding calibration curve of biosensor.

Where $I_{SS}$ (μA) is the steady current, $I_{max}$ (μA) is the current measured when $H_2O_2$ is saturation in PBS solution and $C$ (mmolL$^{-1}$) is the concentration of $H_2O_2$. The apparent Michaelis–Menten constant ($K_M$) is calculated to be 0.292 mM. Compared with other HRP-based $H_2O_2$ biosensors, the value of $K_m^{app}$ is smaller than those of 23.85 mM for HRP immobilized in sol–gel-derived ceramic–carbon nanotube nanocomposite film [44], 23.15 mM for HRP on clay–chitosan–gold nanoparticle nanocomposite modified GC electrode [45], and 5.5 mM for HRP immobilized in polymer [46]. From Table 1, we can see that the complex multiple forklike ZnO nanostructure biosensor shows high sensitivity, rapid response. The good performance of the electrode may be attribute two points: on one hand, the complex multiple forklike ZnO nanostructure provides a high surface area matrix for the enzyme loading; on the other hand, the complex multiple forklike ZnO nanostructure may be preferable for the enzyme and promote the electron transfer between proteins and electrode.

**Table 1**
Comparison of performances between $H_2O_2$ biosensor based on different modified electrode materials.

| Electrode material | Sensitivity (μAm M$^{-1}$) | LOD (μM) | Response time(s) | Ref |
|---|---|---|---|---|
| Nanosized flower-like ZnO | 1.07 | 2 | 5 | 32 |
| Porous nanosheet-based ZnO microspheres | 9.679 | | | 31 |
| Gold nanoparticles | 0.176 | 0.65 | | 47 |
| ZnO particle | 23 | 0.3 | | 48 |
| Complex multiple forklike ZnO nanostructures | 201.12 | 0.3 | 3 | This work |

## 4. Conclusions

In summary, we report here a complex multiple forklike ZnO nanostructure, consisting of a large quantity of nanorods, that are synthesized by citric acid assisted annealing process. These nanorods grow from a thin platelet base and are parallel to each other to form complex multiple forklike ZnO nanostructure. The widthes of thin platelet bases range from 60 to 230 nm. The diameters of the nanorods range from 16 to 60 nm, and their lengths are 0.5μ ~ 1.3μ. Each nanorod of the complex multiple forklike ZnO nanostructure grows along the [0001] direction. The IR spectrum of the complex multiple forklike ZnO nanostructure shows a characteristic absorption band at ~508 cm$^{-1}$ and there will be another absorption band at 432 cm$^{-1}$. These absorption peaks shifted towards lower frequencies when the permittivity of the surrounding medium was increased. This is only one emission peak in the UV region at 384 nm in the room-temperature PL spectra. The absorption spectra have a peak near the band edge in the exciton absorption region (at about 377 nm) and blue-shifted relative to the bulk exciton absorption (380 nm) in UV–Vis absorption spectra. Complex multiple forklike ZnO nanostructure was used to construct a enzymatic biosensor based on the ZnO/CHIT inorganic–organic composite film. The detection limit of the sensor was found to be 0.3 μm. The biosensor could achieve 95% of the steady-state current within 3 s. The linear detection range of complex multiple forklike ZnO nanostructure-based $H_2O_2$ biosensor is $5 \times 10^{-5}$M to $7 \times 10^{-4}$ M with a correction coefficient $R = 0.9979$. The sensitivity of our biosensor is determined to be as high as 201.12 μAm M$^{-1}$, better than many previous reports. The apparent Michaelis–Menten constant ($K_M$) is calculated to be 0.292 mM, which is much lower than that reported. The complex multiple forklike ZnO nanostructure provides an efficient matrix for promoting the electron transfer of proteins and developing biosensors. This enzyme immobilization strategy may hold great potential to be further extended as a general and promising alternative to other bioactive molecules in various biosensor designs.

## Acknowledgements

This work was partly supported from “973” National Key Basic Research Program of China (Grant No. 2006CB604906). Postdoctoral fund of Zhe Jiang province (112200-X90907)

## References

[1] Reynolds DC, Look DC, Jogai B, Hoelscher JE, Sheriff RE, Harris MT, et al. Time-resolved photoluminescence lifetime measurements of the GAMMA_5 and GAMMA_6 free excitons in ZnO. J Appl Phys 2000;88:2152–3.
[2] Tamaki J. High sensitivity semiconductor gas sensors. Sens Lett 2005;3:89–98.
[3] Kurtz M, Strunk J, Hinrichsen O, Muhler M, Fink K, Meyer B, et al. Active sites on oxide surfaces: ZnO-catalyzed synthesis of methanol from CO and $H_2$. Angew Chem Int Ed 2005;44:2790–4.
[4] Cao BQ, Li Y, Duan GT, Cai WP. Growth of ZnO nanoneedle arrays with strong ultraviolet emissions by an electrochemical deposition method. Cryst Growth Des 2006;6:1091–5.
[5] Li YY, Li YX, Wu YL, Sun WL. Preparation and photoluminescent properties of zinc oxide phosphor. J Lumin 2007;126:177–81.
[6] Law M, Greene LE, Goldberger J, Johnson JC, Saykally RJ, Yang P. Nanowire dye-sensitized solar cell. Nat Mater 2005;4:455–9.
[7] Lee SH, Lee SS, Choi JJ, Jeon JU, Ro K. Fabrication of a ZnO piezoelectric micro cantilever with a high-aspect-ratio nano tip. Microsyst Technol 2005;11:416–23.
[8] Clarke DR. Varistor Ceramics. J Am Ceram Soc 1999;82:485–502.

[9] Huang MH, Mao S, Feick H, Yan H, Wu Y, Kind H, et al. room temperature ultraviolet nanolasers. Science 2001;292:1897–9.
[10] Liu B, Zeng HC. Hydrothermal synthesis of ZnO nanorods in the diameter regime of 50 nm. J Am Chem Soc 2003;125:4430–1.
[11] Pan ZW, Dai ZR, Wang ZL. Nanobelts of semiconducting oxides. Science 2001;291:1947–9.
[12] Riaz M, Fulati A, Amin G, Alvi NH, Nur O, Willander M. Buckling and elastic stability of vertical ZnO nanotubes and nanorods. J Appl Phys 2009;106: 034309–034309–6.
[13] Hu JQ, Li Q, Meng XM, Lee CS, Lee ST. Thermal reduction route to the fabrication of coaxial Zn/ZnO nanocables and ZnO nanotubes. Chem Mater 2003;15:305–8.
[14] Milliron DJ, Hughes SM, Cui Y, Manna L, Li JB, Wang LW, et al. Colloidal nanocrystal heterostructures with linear and branched topology. Nature 2004;430:190–5.
[15] Kim GS, Ansari SG, Seo HK, Kim YS, Shin HS. Growth and morphological study of zinc oxide nanoneedles grown on the annealed titanate nanotubes using hydrothermal method. J Appl Phys 2007;102:084302-1–084302–6.
[16] Xiao J, Zhang XX, Zhang GM. Field emission from zinc oxide nanotowers: the role of the top morphology. Nanotechnology 2008;19(29): 295706-1–295706-6.
[17] Yang M, Yin GF, Huang ZB, Kang YQ, Liao XM, Wang H. Preparation and optical properties of biomimic hierarchical ZnO column arrays. Cryst Growth Des 2009;9(2):707–14.
[18] Li HF, Huang YH, Zhang Y, Qi JJ, Yan XQ, Zhang Q, et al. Self-catalytic synthesis, structures, and properties of high-quality tetrapod-shaped ZnO nanostructures. Cryst Growth Des 2009;9(4):1863–8.
[19] Liu JZ, Lee S, Ahn YH, Park JY, Koh KH, Park KH. Identification of dispersion-dependent hexagonal cavity modes of an individual ZnO nanonail. Appl Phys Lett 2008;92:263102-1–263102-3.
[20] Kong XY, Wang ZL. Spontaneous polarization-induced nanohelixes, nanosprings, and nanorings of piezoelectric nanobelts. Nano Lett 2003;3: 1625–31.
[21] Lao CS, Gao PM, Yang SR, Zhang Y, Dai Y, Wang ZL. Formation of double-side teethed nanocombs of ZnO and self-catalysis of Zn-terminated polar surface. Chem Phys Lett 2005;417:359–63.
[22] Lu F, Cai WP. Zhang, YG. ZnO hierarchical micro/nanoarchitectures: solvothermal synthesis and structurally enhanced photocatalytic performance. Adv Funct Mater 2008;18:1047–56.
[23] Kar S, Santra S. ZnO nanotube arrays and nanotube-based paint-brush structures: a simple methodology of fabricating hierarchical nanostructures with self-assembled junctions and branches. J Phys Chem C 2008;112: 8144–6.
[24] Liu ZM, Liu YL, Yang HF, Yang Y, Shen GL, Yu RQ. A mediator-free tyrosinase biosensor based on ZnO sol-gel matrix. Electroanalysis 2005;17:1065–70.
[25] Wang JX, Sun XW, Wei A, Lei Y, Cai XP, Li CM, et al. A zinc oxide nanocomb biosensor for glucose detection. Appl Phys Lett 2006;88:233106-1–233106-3.
[26] Topoglidis E, Campbell CJ, Cass AEG, Durrant JR. Factors that affect protein adsorption on nanostructured titania films: a novel spectroelectrochemical application to sensing. Langmuir 2001;17:7899–906.
[27] Huang IY, Lee MC. Development of a FPW allergy biosensor for human IgE detection by MEMS and cystamine-based SAM technologies. Sens Actuators B Chemical 2008;132:340–8.
[28] Zhang FF, Wang XL, Ai SY, Sun ZD, Wan Q, Zhu ZQ, et al. Immobilization of uricase on ZnO nanorods for a reagentless uric acid biosensor. Anal Chim Acta 2004;519:155–60.
[29] Wei A, Sun XW, Wang JX, Lei Y, Cai XP, Li CM, et al. Enzymatic glucose biosensor based on ZnO nanorod array grown by hydrothermal decomposition. Appl Phys Lett 2006;89:123902-1–123902-3.
[30] Chen LY, Gu BX, Zhu GP, Wu YF, Liu SQ, Xu CX. Tyrosinase biosensor based on zinc oxide nanorods. Nano 2007;2:281–4.
[31] Lu XB, Zhang HJ, Ni YW, Zhang Q, Chen JP. Porous nanosheet-based ZnO microspheres for the construction of direct electrochemical biosensors. Biosens Bioelectron 2008;24:93–8.
[32] Liu YL, Yang YH, Yang HF, Liu ZM, Shen GL, Yu RQ. Nanosized flower-like ZnO synthesized by a simple hydrothermal method and applied as matrix for horseradish peroxidase immobilization for electro-biosensing. J Inorg Biochem 2005;99:2046–53.
[33] Tasker PW. The stability of ionic crystal surfaces. J Phys C Solid State Phys 1979;12:4977–84.
[34] Peng ZA, Peng XG. Nearly monodisperse and shape-controlled CdSe nanocrystals via alternative routes: nucleation and growth. J Am Chem Soc 2002;124:3343–53.
[35] Peng ZA, Peng XG. Mechanisms of the shape evolution of CDSe nanocrystals. J Am Chem Soc 2001;123:1389–95.
[36] Verges MA, Mifsud A, Serna CJ. Formation of rod-like zinc oxide microcrystals in homogeneous solutions. J Chem Soc Faraday Trans 1990;86(6):959–63.
[37] Sigoli FA, Davolos MR, Jafelicci M. Morphological evolution of zinc oxide originating from zinc hydroxide carbonate. J Alloys Comp 1997;262:292–5.
[38] Hsu NE, Hung WK, Chen YF. Origin of defect emission identified by polarized luminescence from aligned ZnO nanorods. J Appl Phys 2004;96:4671–3.
[39] Shalish I, Temkin H, Narayanamurti V. Sizedependent surface luminescence in ZnO nanowires. Phys Rev B 2004;69:245401–4.
[40] Vanheusden K, Warren WL, Seager CH, Tallant DR, Voigt JA, Gnade BE. Mechanisms behind green photoluminescence in ZnO phosphor powders. J Appl Phys 1996;79:7983–90.
[41] Ziegler E, Heinrich A, Oppermann H, Stover G. Electrical properties and nonstoichiometry in ZnO single crystals. Phys Status Solidi A 1981;66:635–48.
[42] Liu GD, Wu ZY, Wang SP, Shen GL, Yu RQ. Renewable amperometric immunosensor for schistosoma japonicium antibody assay. Anal Chem 2001;73: 3219–26.
[43] Kamin RA, Wilson GS. Rotating ring-disk enzyme electrode for biocatalysis kinetic studies and characterization of the immobilized enzyme layer. Anal Chem 1980;52:1198–205.
[44] Chen HJ, Dong SJ. Direct electrochemistry and electrocatalysis of horseradish peroxidase immobilized in sol-gel-derived ceramic-carbon nanotube nanocomposite film. Biosens Bioelectron 2007;22:1811–5.
[45] Zhao X, Mai Z, Kong X, Zou X. Direct electrochemistry and electrocatalysis of horseradish peroxidase based on clay-chitosan-gold nanoparticle nanocomposite. Biosens Bioelectron 2008;23:1032–8.
[46] Xu Z, Cao N, Chen HJ, Dong SJ. Biopolymer and carbon nanotubes interface prepared by self-assembly for studying the electrochemistry of microperoxidase-11. Langmuir 2005;21:10808–13.
[47] Tangkuaram T, Ponchio C, Kangkasomboon T, Katikawong P, Veerasai W. Design and development of a highly stable hydrogen peroxide biosensor on screen printed carbon electrode based on horseradish peroxidase bound with gold nanoparticles in the matrix of chitosan. Biosens Bioelectron 2007;22: 2071–8.
[48] Zhu XL, Yuri I, Gan X, Suzuki I, Li GX. Electrochemical study of the effect of nano-zinc oxide on microperoxidase and its application to more sensitive hydrogen peroxide biosensor preparation. Biosens Bioelectron 2007;22: 1600–4.